4 May 2007 | $10

Science

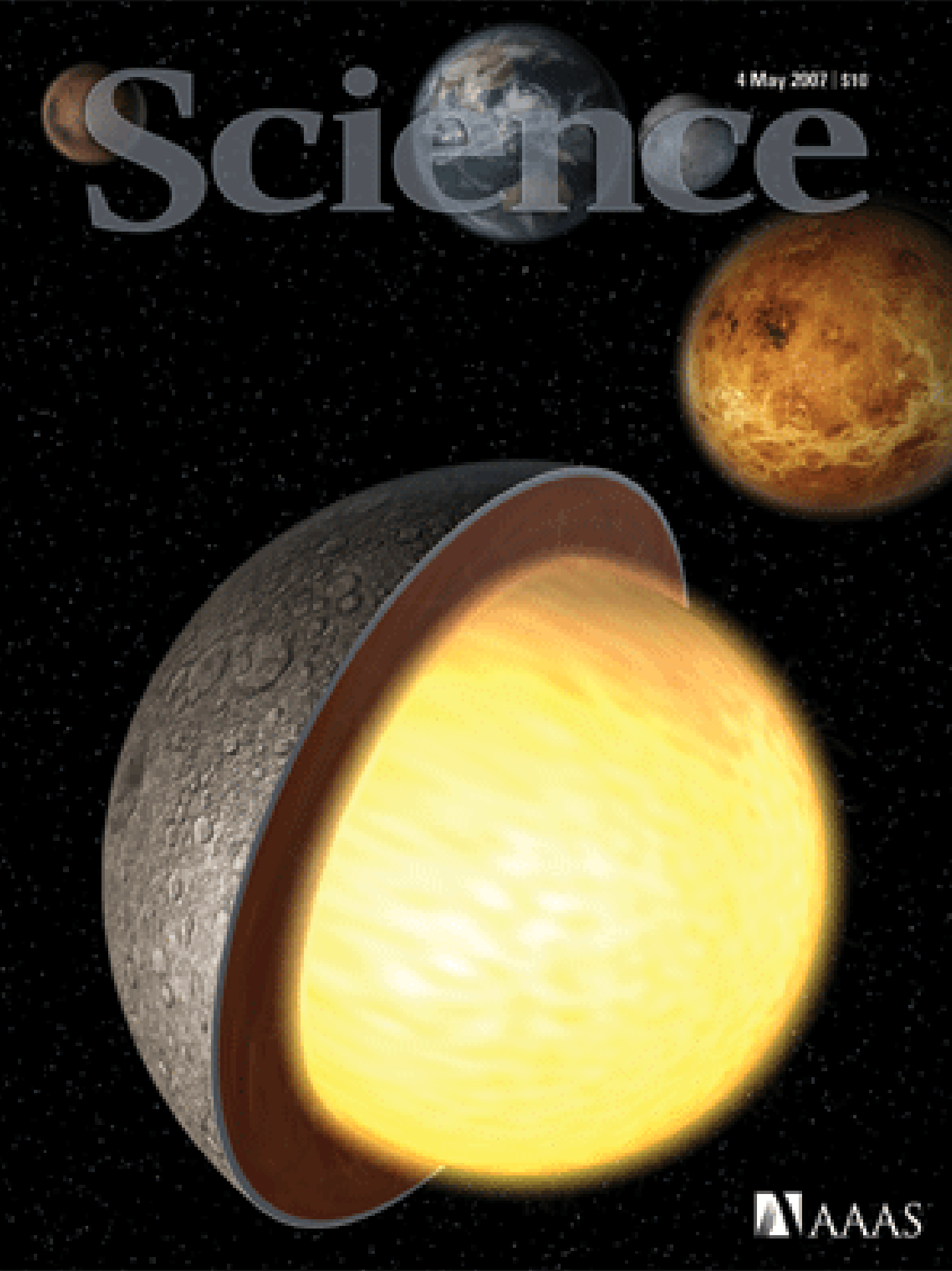

AAAS

Synthesis of Tetrahexahedral Platinum Nanocrystals with High-Index Facets and High Electro-Oxidation Activity

Na Tian, *et al.*

Science **316**, 732 (2007);
DOI: 10.1126/science.1140484

Science (print ISSN 0036-8075; online ISSN 1095-9203) is published weekly, except the last week in December, by the American Association for the Advancement of Science, 1200 New York Avenue NW, Washington, DC 20005.

can lower the Au nucleation temperature by roughly 40 K, and a 4% increase in Ge might stabilize the liquid phase against Au nucleation at temperatures as low as 260°C. Such large kinetically driven supersaturations are not expected in typical macroscopic systems but become increasingly likely in strongly facetted systems as they shrink to the nanoscale (*28*, *31*). The degree of supersaturation would increase with growth rate, which could explain the successful growth of Ge nanowires at temperatures as low as 260°C in conventional chemical vapor deposition, where the growth rate is far higher than that in our experiments.

In conclusion, we have shown that during the growth of Ge wires using Au, the catalyst state may be either solid or liquid below T_e, with the state depending not just on temperature but also on Ge_2H_6 pressure and history. Nanowire growth continues regardless of the state the catalyst is in. In other words, both VLS and VSS processes can operate under the same conditions to grow Ge wires. A substantial Ge_2H_6 pressure is essential for growth via VLS below T_e. We propose a possible mechanism for the existence of a liquid catalyst at these temperatures, which is consistent with the observed dependence on Ge_2H_6 pressure and wire diameter. These results demonstrate that source gas pressure, though generally not considered a key factor, is actually crucial in determining the growth mode. The role of growth pressure and history may be relevant to controlling nanowire synthesis below T_e and to resolving the controversy surrounding the catalyst state in other materials systems.

References and Notes

1. K. Haraguchi, T. Katsuyama, K. Hiruma, K. Ogawa, *Appl. Phys. Lett.* **60**, 745 (1992).
2. J. Hu, T. W. Odom, C. M. Lieber, *Acc. Chem. Res.* **32**, 435 (1999).
3. L. Samuelson, *Mater. Today* **6**, 22 (2003).
4. H. J. Fan, P. Werner, M. Zacharias, *Small* **2**, 700 (2006).
5. R. S. Wagner, W. C. Ellis, *Appl. Phys. Lett.* **4**, 89 (1964).
6. Y. Wang, V. Schmidt, S. Senz, U. Gösele, *Nat. Nanotechnol.* **1**, 186 (2006).
7. Y. Yao, S. Fan, *Mater. Lett.* **61**, 177 (2007).
8. T. I. Kamins, R. S. Williams, D. P. Basile, T. Hesjedal, J. S. Harris, *J. Appl. Phys.* **89**, 1008 (2001).
9. G. A. Bootsma, H. J. Gassen, *J. Cryst. Growth* **10**, 223 (1971).
10. Y. Miyamoto, M. Hirata, *Jpn. J. Appl. Phys.* **14**, 1419 (1975).
11. D. Wang, H. Dai, *Angew. Chem. Int. Ed.* **41**, 4783 (2002).
12. T. I. Kamins, X. Li, R. S. Williams, *Nano Lett.* **4**, 503 (2004).
13. A. B. Greytak, L. J. Lauhon, M. S. Gudiksen, C. M. Lieber, *Appl. Phys. Lett.* **84**, 4176 (2004).
14. H. Adhikari, A. F. Marshall, C. E. D. Chidsey, P. C. McIntyre, *Nano Lett.* **6**, 318 (2006).
15. K. Hiruma *et al.*, *J. Appl. Phys.* **77**, 447 (1995).
16. A. I. Persson *et al.*, *Nat. Mater.* **3**, 677 (2004).
17. J. C. Harmand *et al.*, *Appl. Phys. Lett.* **87**, 203101 (2005).
18. M. Tchernycheva, J. C. Harmand, G. Patriarche, L. Travers, G. E. Cirlin, *Nanotechnology* **17**, 4025 (2006).
19. K. A. Dick *et al.*, *Nano Lett.* **5**, 761 (2005).
20. H. D. Park, A.-C. Gaillot, S. M. Prokes, R. C. Cammarata, *J. Cryst. Growth* **296**, 159 (2006).
21. S. Kodambaka, J. Tersoff, M. C. Reuter, F. M. Ross, *Phys. Rev. Lett.* **96**, 096105 (2006).
22. O. G. Shpyrko *et al.*, *Science* **313**, 77 (2006).
23. Q. Xu *et al.*, *Phys. Rev. Lett.* **97**, 155701 (2006).
24. F. M. Ross, J. Tersoff, M. C. Reuter, *Phys. Rev. Lett.* **95**, 146104 (2005).
25. F. Glas, J.-C. Harmand, *Phys. Rev. B* **73**, 155320 (2006).
26. Using 160 kJ/mol for the heat of reaction $Ge_2H_6 \rightarrow 2Ge + 3H_2$ (*32*) and a thermal conductivity of 5 W/mK for a 20-nm-wide wire, and assuming that all heat is conducted away, we estimate a maximum temperature difference ΔT of $\sim 10^{-5}$ K between the base and the tip of a 1-μm-long wire growing at 10^{-5} Torr of Ge_2H_6. In case of heat loss through radiation to the ambient, $\Delta T \sim 10^{-2}$ K.
27. N. Mingo, L. Yang, D. Li, A. Majumdar, *Nano Lett.* **3**, 1713 (2003).
28. S. D. Peteves, R. Abbaschian, *Metall. Trans. A* **22A**, 1259 (1991).
29. T. B. Massalski, J. L. Murray, L. H. Bennett, H. Baker, Eds. *Binary Alloy Phase Diagrams* (American Society for Metals, Metals Park, OH, 1986), vol. 1, pp. 263–264.
30. J. L. Taraci *et al.*, *Appl. Phys. Lett.* **84**, 5302 (2004).
31. M. J. Aziz, in *The Selected Works of John W. Cahn*, W. C. Carter, W. C. Johnson, Eds. (Minerals, Metals, and Materials Society, Warrendale, PA, 1998), pp. 207–209.
32. D. R. Lide, Ed., *CRC Handbook of Chemistry and Physics* (CRC Press, Boca Raton, FL, 2005).

33. We acknowledge R. M. Tromp, S. Guha, M. A. Aziz, and E. Tutuc for helpful discussions; A. Ellis for the development of in situ microscopy facilities; and L. Gignac and K. B. Reuter for energy-dispersive x-ray and electron energy-loss spectroscopy analyses of the wires. This work was partially supported by Defense Advanced Research Projects Agency (DARPA) under contract N66001-05-C-6030.

Supporting Online Material

www.sciencemag.org/cgi/content/full/316/5825/729/DC1
Fig. S1

20 December 2006; accepted 21 March 2007
10.1126/science.1139105

Synthesis of Tetrahexahedral Platinum Nanocrystals with High-Index Facets and High Electro-Oxidation Activity

Na Tian,[1] Zhi-You Zhou,[1] Shi-Gang Sun,[1]* Yong Ding,[2] Zhong Lin Wang[2]*

The shapes of noble metal nanocrystals (NCs) are usually defined by polyhedra that are enclosed by {111} and {100} facets, such as cubes, tetrahedra, and octahedra. Platinum NCs of unusual tetrahexahedral (THH) shape were prepared at high yield by an electrochemical treatment of Pt nanospheres supported on glassy carbon by a square-wave potential. The single-crystal THH NC is enclosed by 24 high-index facets such as {730}, {210}, and/or {520} surfaces that have a large density of atomic steps and dangling bonds. These high-energy surfaces are stable thermally (to 800°C) and chemically and exhibit much enhanced (up to 400%) catalytic activity for equivalent Pt surface areas for electro-oxidation of small organic fuels such as formic acid and ethanol.

Generally, catalytic performance of nanocrystals (NCs) can be finely tuned either by their composition, which mediates electronic structure (*1*, *2*), or by their shape, which determines surface atomic arrangement and coordination (*3*, *4*). Fundamental studies of single-crystal surfaces of bulk Pt have shown that high-index planes generally exhibit much higher catalytic activity than that of the most common stable planes, such as {111}, {100}, and even {110}, because the high-index planes have a high density of atomic steps, ledges, and kinks, which usually serve as active sites for breaking chemical bonds (*5*–*7*). For example, a bulk Pt(210) surface possesses extremely high catalytic reactivity for electroreduction of CO_2 (*8*) and electro-oxidation of formic acid (*9*). The bulk Pt(410) surface exhibits unusual activity for catalytic decomposition of NO, a major pollutant of automobile exhaust (*10*). Thus, the shape-controlled synthesis of metal NCs bounded by high-index facets is a potential route for enhancing their catalytic activities.

It is, however, rather challenging to synthesize shape-controlled NCs that are enclosed by high-index facets because of their high surface energy. Crystal growth rates in the direction perpendicular to a high-index plane are usually much faster than those along the normal direction of a low-index plane, so high-index planes are rapidly eliminated during particle formation (*11*). During the past decade, a variety of face-centered cubic (fcc) structured metal NCs with well-defined shapes have been synthesized, but nearly all of them are bounded by the low-index planes, such as tetrahedron, octahedron, decahedron, and icosahedron, enclosed by {111} facets (*12*–*14*), cube by {100} (*12*, *15*), cuboctahedron by {111} and {100} (*16*), and rhombic dodecahedron by {111} (*17*). Here we describe an electrochemical method for the synthesis of tetrahexahedral (THH) Pt NCs at high purity. The THH shape is bounded by 24 facets of high-index planes ~{730} and vicinal planes such as {210}

[1]State Key Laboratory of Physical Chemistry of Solid Surfaces, Department of Chemistry, College of Chemistry and Chemical Engineering, Xiamen University, Xiamen 361005, China. [2]School of Materials Science and Engineering, Georgia Institute of Technology, Atlanta, GA 30332–0245, USA.

*To whom correspondence should be addressed. E-mail: sgsun@xmu.edu.cn (S.G.S.); zhong.wang@mse.gatech.edu (Z.L.W.)

and {310}. The synthesized THH Pt NCs show enhanced catalytic activity in electro-oxidation of small organic fuels of formic acid and ethanol, demonstrating their potential for use in the traditional applications of Pt group metal nanoparticles, including catalysts (*18*), automotive catalytic converters (*19*), fuel cells (*20*), and sensors (*21*).

Several electrochemical methods have been reported for the synthesis of Pt NCs. Sun and coworkers used a fast potential cycling to grow nanostructured film on a Pt microelectrode surface (*22*), and Arvia *et al.* employed an electrochemical square-wave potential route to shape bulk Pt electrode (*23*), which could yield several high-index planes of bulk crystals in some cases (*24*). However, these methods have limited practical applications because of a low specific surface area and the high cost of the bulk Pt electrode. We have developed a route for shape-controlled synthesis of Pt NCs through a square-wave potential. Starting from Pt nanospheres electrodeposited on glassy carbon (GC) substrate instead of bulk Pt, we obtained THH Pt NCs at high yield. Electrochemical preparation was carried out in a standard three-electrode cell at room temperature (*25*). All electrode potentials are reported on the scale of a saturated calomel electrode (SCE). In a typical experiment, polycrystalline Pt nanospheres of size about 750 nm (fig. S1) were electrodeposited on a GC electrode in a solution of 2 mM K_2PtCl_6 + 0.5 M H_2SO_4. The Pt nanospheres were then subjected to a square-wave treatment, with upper potential 1.20 V and lower potential between –0.10 and –0.20 V, at 10 Hz in a solution of 0.1 M H_2SO_4 + 30 mM ascorbic acid for 10 to 60 min. As illustrated schematically by Fig. 1A, THH Pt NCs were grown exclusively on GC surface at the expense of Pt nanospheres.

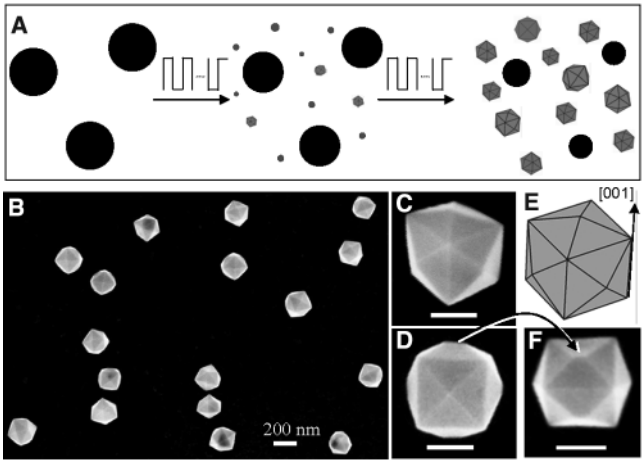

Fig. 1. (**A**) Scheme of electrochemical preparation of THH Pt NCs from nanospheres. The Pt nanosphere is an agglomeration of tiny Pt nanoparticles of irregular shapes (fig. S1). Under the influence of the square-wave potential, new Pt NCs of THH shape grow at the expense of the large nanospheres (the large nanosphere is "dissolved" into smaller ones, which eventually transform into THH shape). (**B**) Low-magnification SEM image of THH Pt NCs with growth time of 60 min. (**C** and **D**) High-magnification SEM images of Pt THH viewed down along different orientations, showing the shape of the THH. (**E**) Geometrical model of an ideal THH. (**F**) High-magnification SEM image of a THH Pt NC, showing the imperfect vertices as a result of unequal size of the neighboring facets. Scale bars in (C), (D), and (F), 100 nm.

The shape of the NCs was determined initially by scanning electron microscopy (SEM). An SEM image of THH Pt NCs produced with a growth time of 60 min is shown in Fig. 1B (an overview SEM image including THH Pt NCs and residual Pt nanospheres is shown in fig. S2). The yield of the THH Pt NCs in the final product is >90%, and most other shapes are an agglomeration of imperfect THH NCs (fig. S3). Their average size (Heywood diameter) was 217 nm, with a standard deviation of 23 nm. By controlling the experimental conditions, the smallest THH NCs received and identified by SEM are ~20 nm (fig. S3). The THH Pt NCs on GC surface are randomly oriented. High-magnification SEM images of THH Pt NCs oriented nearly along the three- and four-fold axes are presented in Fig. 1, C and D, respectively.

The THH shape is based on a cube with each face capped by a square-based pyramid (Fig. 1E). Three perfect square-based pyramids in Fig. 1C and nearly octagonal projection in Fig. 1D can be seen clearly, which confirms the THH shape of the Pt NC. In some cases, imperfection can be introduced at vertices (fig. S4), as presented by the SEM image in Fig. 1D, which is not caused by the {100} truncation of the THH but rather because crystal facets of different sizes are produced by substrate effects (Fig. 1F). Transmission electron microscopy (TEM) analysis of such structure clearly reveals the three-dimensional (3D) structure of the NC (fig. S5). In comparison with previous electrochemical faceting of bulk Pt electrodes (*24*), the use of Pt nanospheres deposited on GC substrate is vital to the production of nearly perfect THH Pt NCs, because GC is an inert substrate on which isolated Pt NCs grow in island (Volmer-Weber) mode but not columnar mode (*26*).

THH-shaped crystals in nature exist occasionally in fluorite and diamond but very rarely in metals. To the best of our knowledge, only copper crystals of truncated THH shape were found in copper minerals (*27*). The THH (O_h symmetry) belongs to Catalan solids or Archimedean duals; the THH shape is bounded by 24 high-index planes of {hk0} (h≠k≠0) (*28*). We determined the facets of the THH Pt NCs by selected-area electron diffraction (SAED) and high-resolution TEM (HRTEM).

The facets are best revealed by imaging the NC along [001], parallel to which 8 of the 24 facets are imaged edge-on (Fig. 2, A and B).

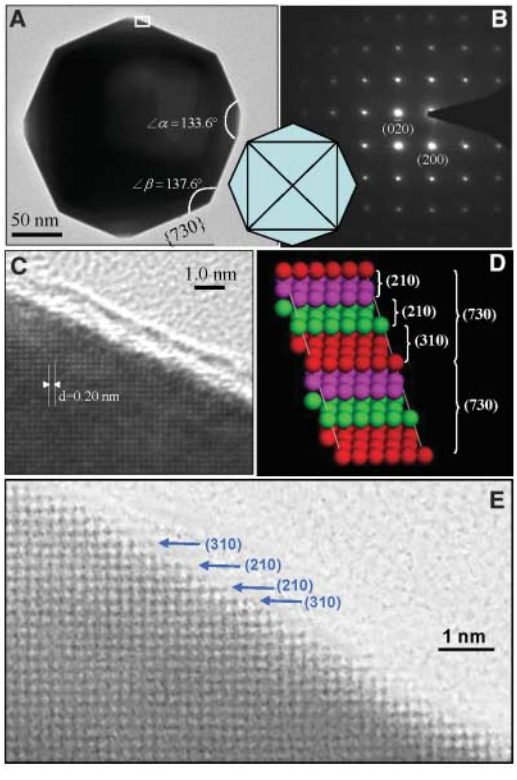

Fig. 2. (**A**) TEM image of THH Pt NC recorded along [001] direction. A careful measurement of the angles between surfaces indicates that the profiles of the exposed surfaces are {730} planes (α = 133.6°, β = 136.4°) (see fig. S6). The inset is a [001] projected model of the THH. (**B**) Corresponding SAED pattern with square symmetry, showing the single-crystal structure of the THH Pt NC. (**C**) High-resolution TEM image recorded from the boxed area marked in (A). An amorphous thin layer is shown at the surface, which may be introduced by contamination during specimen handling and/or TEM observation. (**D**) Atomic model of Pt(730) plane with a high density of stepped surface atoms. The (730) surface is made of (210) and (310) subfacets. The local surface of THH Pt NC can be (210) if the size of the crystal surface increases, although the overall profile of the facets is (730). (**E**) HRTEM image recorded from another THH Pt NC to reveal surface atomic steps in the areas made of (210) and (310) subfacets. The image reveals the surface atomic steps.

The fourfold symmetry of the SAED pattern confirms that the THH Pt NC is a single crystal. The HRTEM image in Fig. 2C recorded from a boxed area in Fig. 2A shows continuous lattice fringes with lattice spacing of 0.20 nm, which corresponds to the {200} planes of Pt. The Miller indices of exposed facets of the THH can be identified by a conjunction of the angles between the facets, the TEM image, and the ED pattern of the Pt NC (Fig. 2, A and B), whose border can be looked at as the projection of eight {hk0} facets parallel to the [001] zone axis. As shown in Fig. 2A, two surface angles of 133.6 ± 0.3° and 137.6 ± 0.3° are measured, which are in good agreement with theoretical values of angle α = 133.6° and angle β = 136.4° between {730} facets (fig. S6). The results show that the dominant facets of the THH Pt NC are {730}. Although most of the THH Pt NCs are bounded by the {730} facets, some THH Pt NCs bounded by {210}, {310}, or {520} had also been observed [fig. S7 (*25*)].

The atomic arrangement of the Pt(730) surface (Fig. 2D) is periodically composed of two (210) subfacets followed by one (310) subfacet, that is, a multiple-height stepped structure (*6*). These steps have been directly captured in an HRTEM image recorded from another THH, as indicated by arrows in Fig. 2E. Thus, the single-crystal THH is enclosed by 24 high-index facets of ~{730}.

In addition to the HRTEM results, the surface structure of THH Pt NCs can also be characterized by cyclic voltammograms (fig. S8), in which the features of oxygen adsorption and desorption are similar to those on a bulk Pt(210) surface but are different from those on a polycrystalline Pt surface. In a common point, these high-index facets exhibit an open structure. In the case of a Pt(730) surface, its density of stepped atoms is as high as 5.1×10^{14} cm^{-2}, that is, 43% of the total number of atoms on the surface. It is thus reasonable to expect that the THH Pt NCs will display high catalytic activity.

The size of the THH Pt NCs can be controlled by varying the growth time. The SEM images of THH Pt NCs produced with growth times of 10, 30, 40, and 50 min are shown in Fig. 3, A to D, respectively. The corresponding average sizes are measured, respectively, to be 53, 100, 126, and 144 nm. The histograms of size distributions of these particles are shown in Fig. 3E, with a relative standard deviation (RSD) of 12%, 10%, 14%, and 14%, respectively. The particle size is also correlated with the density of THH Pt NCs on the substrate surface. The (210) and (310) planes, the major subfacets for composing of the (730) as shown in Fig. 2D, exhibited high stability under electrochemical conditions and solid-gas environments in both oxidative and reducing atmospheres (*9*, *29*–*31*). The THH Pt NCs are thermally stable; in situ TEM observation showed that the THH Pt NCs were thermally stable to temperatures of ~800°C with the preservation of the shape and facets (Fig. 3F). (Note the large size of the particles.)

Why are the {730} or the {210} type of facets that define the THH shape stable during growth? We have found that ascorbic acid is not the intrinsic reason to produce the THH shape, because THH Pt NCs can still be harvested in ascorbic acid–free solution, although the yield and quality degrade (fig. S9). In the original synthesis procedures (Fig. 1A), the initial stage of treating the nanospheres by square-wave potential, the following processes may occur (*25*). First, at 1.20 V, the surface Pt atoms on the nanospheres can be oxidized and partially dissolved to form Pt ions. Then, these Pt ions diffuse to the GC surface and are reduced to Pt atoms between –0.20 and –0.10 V. In the square-wave potential procedure, the two processes were repeated periodically at a frequency of 10 Hz, and new Pt NCs grow through nucleation and growth on GC surface with a continuous dissolving of the original Pt nanospheres, because the small nanoparticles grow more rapidly than the larger ones (*32*).

It has been reported that the surface structure of Pt single crystals could be changed by periodic adsorption and desorption of oxygen, depending on their Miller indices (*33*). At 1.20 V, Pt surface is oxidized and covered by oxygen species (O_{ad} and OH_{ad}) originated from the dissociation of H_2O in solution. As for the low-energy planes, surface atoms have larger coordination numbers (CNs), such as 9 for atoms on the (111) plane, so oxygen atoms are relatively difficult to adsorb at such surface sites; instead, some oxygen atoms might preferentially diffuse or invade into a Pt surface to form a Pt-O lattice through place-exchange between oxygen and Pt atoms. After reduction between –0.20 and –0.10 V, these displaced Pt atoms cannot always return to their original positions because the synthesis was carried out at room temperature, which then disorders surface structure (*33*). However, for high-index planes, the CNs of surface atoms are relatively low, only 6 for stepped atoms on the {730} plane. The oxygen atoms preferentially adsorb at such stepped atoms without replacing them, and ordered surfaces are preserved (*33*, *34*). The dynamic oxygen adsorption-desorption mediated by square-wave potential and the different degrees of place-exchange between oxygen and Pt atoms on Pt single-crystal surfaces show that only high-index planes with an open structure, such as the {730} and {210} facets, can survive in the treatment of square-wave potential (fig. S10).

The catalytic activity of THH Pt NCs is superior to that of the spherical Pt nanoparticles. The NCs have been applied to promote the electro-oxidation of formic acid and ethanol, which are promising alternative fuels for direct fuel cells. Figure 4A shows a comparison of transient current density of formic acid oxidation at 0.25 V on the THH Pt NCs [$\overline{d}$ = 81 nm (fig. S11)], the electrodeposited polycrystalline Pt nanospheres [$\overline{d}$ = 115 nm (fig. S12)], and the commercial 3.2-nm Pt/C catalyst from E-TEK, Inc. (Somerset, New Jersey, USA) (fig. S13) at room temperature. The oxidation current has been normalized to electroactive Pt surface area so that the current density (*j*) can be directly used

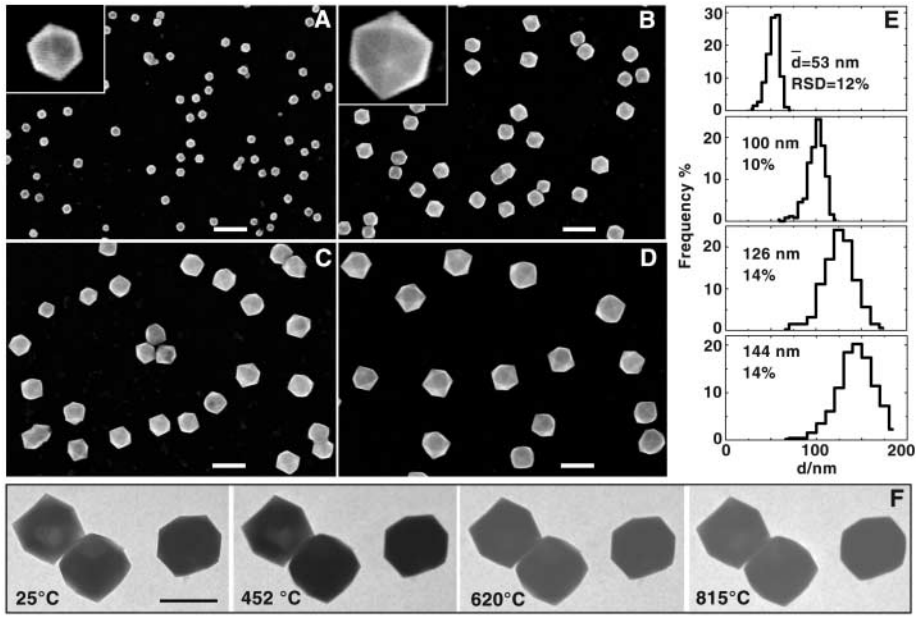

Fig. 3. Size control of THH Pt NCs and their thermal stability. SEM images of THH Pt NCs grown at (**A**) 10, (**B**) 30, (**C**) 40, and (**D**) 50 min. The insets in (A) and (B) are the high-magnification SEM images that confirm the shape of THH. Scale bars, 200 nm. (**E**) Size distributions of THH Pt NCs in (A), B), (C), and (D), respectively, after counting more than 500 particles for each sample. (**F**) In situ TEM observation on the thermal stability of THH Pt NCs. The images were recorded at various temperatures in TEM at a heating rate of 7°C/min. The NC preserves its shape to ~815°C and even higher with a slight truncation at the corners and apexes, as seen in the TEM image.

to compare the catalytic activity of different samples (*25*). The oxidation current density on THH Pt NCs is nearly double that on Pt nanospheres or Pt/C catalyst. The potential dependence of the steady-state current density recorded at 60 s is shown in Fig. 4B. The current density of formic acid oxidation on THH Pt NCs is higher than that on the Pt nanospheres or the Pt/C catalyst, and the enhancement factor *R*, which is defined as the ratio of the current density measured on THH Pt NCs versus that acquired on Pt nanospheres or Pt/C catalyst, varies from 160% to 400% for Pt nanospheres and from 200% to 310% for Pt/C catalyst, depending on electrode potential. The THH Pt NC showed no appreciable morphological change after the reaction, as indicated by an SEM image of a THH Pt NC inset in Fig. 4B, which still preserves the THH shape, showing its chemical stability.

For ethanol oxidation, the transient current density on THH Pt NCs at 0.30 V is enhanced to 230% of that on the nanospheres and 330% of that on the Pt/C catalyst (Fig. 4C). A comparison of the steady-state current densities obtained on THH Pt NCs, Pt nanospheres, and 3.2-nm commercial Pt/C catalyst is shown in Fig. 4D, in which the enhancement factor *R* varies between 200% and 430% for Pt nanospheres and between 250% and 460% for Pt/C catalyst in the potential region of 0.20 to 0.55 V. In addition, we have measured that, at a given oxidation current density of technical interest in fuel cell application, as indicated by dashed lines in Fig. 4, B and D, the corresponding potential on THH Pt NCs is much lower than that on Pt nanospheres or Pt/C catalyst. In the case of formic acid oxidation, the potential on THH Pt NCs is shifted negatively by ~60 mV as compared with Pt nanospheres at the same current density of 0.5 mA cm^{-2}, whereas for ethanol oxidation, the negative shift is ~80 mV at a current density of 0.2 mA cm^{-2}. The above results show that THH Pt NCs exhibit much enhanced catalytic activity per unit surface area for the oxidation of small organic molecules. This may be attributed to the high density of stepped atoms on the surfaces of THH Pt NCs. However, for catalytic activity per unit weight of Pt, our estimation indicates that, when the transformation is complete, the overall activity of these larger THH NCs is less than that of the 3-nm commercial Pt nanoparticles (~10% as active). Future research will be needed to improve the synthesis technique so that smaller-size THH NCs are made in high yield and still consume almost all of the starting Pt nanoparticles.

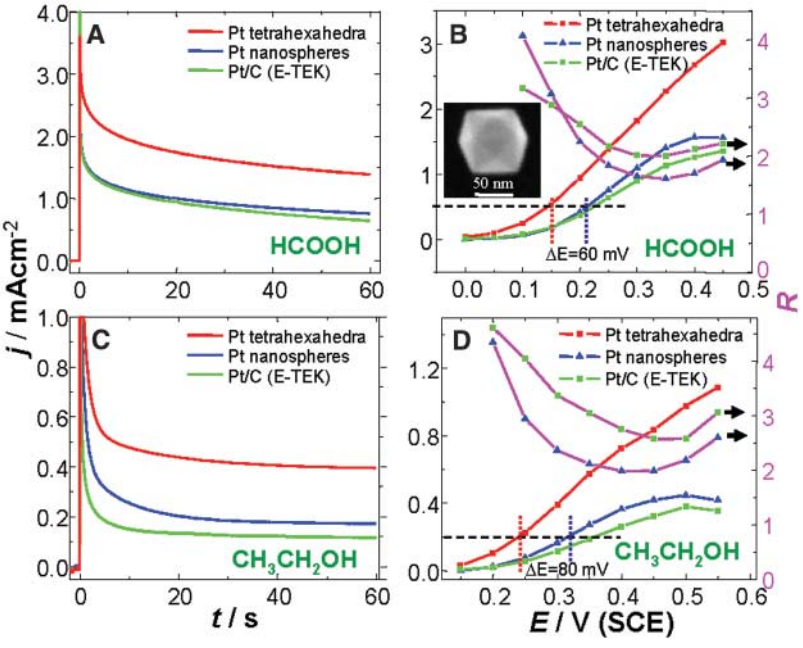

Fig. 4. Comparison of catalytic activity per unit Pt surface area among THH Pt NCs, polycrystalline Pt nanospheres, and 3.2-nm Pt/C catalyst. (**A**) Transient current density curves of formic acid oxidation at 0.25 V. (**B**) Potential-dependent steady-state current density (left, recorded at 60 s) of formic acid oxidation on THH Pt Ncs, Pt nanospheres, and commercial Pt/C catalyst, and the ratios *R* (right) between that of THH with the latter two, respectively. The inset in (B) is an SEM image of a THH Pt NC after reaction, indicating the preservation of shape. (**C**) Transient current density curves of ethanol oxidation at 0.30 V for the THH, Pt nanospheres, and Pt/C catalyst. (**D**) Potential-dependent steady-state current density (left) of ethanol oxidation on THH Pt NCs, Pt nanospheres, and commercial Pt/C catalyst, and the ratios *R* (right). The current density *j* was normalized in reference to the electrochemical active surface area for each sample, so that the current density *j* directly corresponds to the catalytic activity of unit Pt surface area of the sample. Thus, it can be directly compared for three types of particles. The results clearly demonstrate the largely enhanced catalytic activities of the THH Pt NCs per unit surface area.

References and Notes

1. J. Zhang, K. Sasaki, E. Sutter, R. R. Adzic, *Science* **315**, 220 (2007).
2. V. R. Stamenkovic *et al.*, *Science* **315**, 493 (2007).
3. R. Narayanan, M. A. El-Sayed, *Nano Lett.* **4**, 1343 (2004).
4. F. J. Vidal-Iglesias *et al.*, *Electrochem. Commun.* **6**, 1080 (2004).
5. G. A. Somorjai, D. W. Blakely, *Nature* **258**, 580 (1975).
6. G. A. Somorjai, *Chemistry in Two Dimensions: Surfaces* (Cornell University Press, Ithaca, NY, 1981).
7. S. G. Sun, A. C. Chen, T. S. Huang, J. B. Li, Z. W. Tian, *J. Electroanal. Chem.* **340**, 213 (1992).
8. N. Hoshi, S. Kawatani, M. Kudo, Y. Hori, *J. Electroanal. Chem.* **467**, 67 (1999).
9. S. G. Sun, J. Clavilier, *Chem. J. Chin. Univ.* **11**, 998 (1990).
10. W. F. Banholzer, R. I. Masel, *J. Catal.* **85**, 127 (1984).
11. H. E. Buckley, *Crystal Growth* (Wiley, New York, 1951).
12. T. S. Ahmadi, Z. L. Wang, T. G. Green, A. Henglein, M. A. El-Sayed, *Science* **272**, 1924 (1996).
13. F. Kim, S. Connor, H. Song, T. Kuykendall, P. D. Yang, *Angew. Chem. Int. Ed.* **43**, 3673 (2004).
14. Y. J. Xiong, J. M. McLellan, Y. D. Yin, Y. N. Xia, *Angew. Chem. Int. Ed.* **46**, 790 (2007).
15. Y. Sun, Y. Xia, *Science* **298**, 2176 (2002).
16. H. Song, F. Kim, S. Connor, G. A. Somorjai, P. D. Yang, *J. Phys. Chem. B* **109**, 188 (2005).
17. X. G. Liu, N. Q. Wu, B. H. Wunsch, R. J. Barsotti, F. Stellacci, *Small* **2**, 1046 (2006).
18. A. Wieckowski, E. Savinova, C. G. Vayenas (Eds.), *Catalysis and Electrocatalysis at Nanoparticle Surfaces* (Marcel Dekker, Inc., New York, 2003).
19. R. M. Heck, R. J. Farrauto, *Appl. Catal. Gen.* **221**, 443 (2001).
20. J. Larminie, A. Dicks, *Fuel Cell Systems Explained, 2nd Edition* (Wiley, Chichester, West Sussex, 2003).
21. F. Favier, E. C. Walter, M. P. Zach, T. Benter, R. M. Penner, *Science* **293**, 2227 (2001).
22. H. Gong, S. G. Sun, Y. J. Chen, S. P. Chen, *J. Phys. Chem. B* **108**, 11575 (2004).
23. A. Visintin, J. C. Canullo, W. E. Triaca, A. J. Arvia, *J. Electroanal. Chem.* **239**, 67 (1988).
24. W. A. Egli, A. Visintin, W. E. Triaca, A. J. Arvia, *Appl. Surf. Sci.* **68**, 583 (1993).
25. Materials and methods are available as supporting material on *Science* Online.
26. G. H. Gilmer, H. Huang, C. Roland, *Comput. Mater. Sci.* **12**, 354 (1998).
27. A. E. Seaman Mineral Museum of Michigan Technological University (available at www.museum.mtu.edu/Gallery/copper.html).
28. A. A. Proussevitch, D. L. Sahagian, *Comput. Geosci.* **27**, 441 (2001).
29. S. G. Sun, D. F. Yang, S. J. Wu, J. Ociepa, J. Lipkowski, *J. Electroanal. Chem.* **349**, 211 (1993).
30. D. W. Blakely, G. A. Somorjai, *Surf. Sci.* **65**, 419 (1977).
31. P. J. Knight, S. M. Driver, D. P. Woodruff, *Chem. Phys. Lett.* **259**, 503 (1996).
32. H. Reiss, *J. Chem. Phys.* **19**, 482 (1951).
33. N. Furuya, M. Shibata, *J. Electroanal. Chem.* **467**, 85 (1999).
34. A. V. Tripkovic, R. R. Adzic, *J. Electroanal. Chem.* **205**, 335 (1986).

35. This work was supported by grants from the Natural Science Foundation of China (20433060, 20503023, and 20673091) and Special Funds for Major State Basic Research Project of China (2002CB211804). Y.D. and Z.L.W. were supported by U.S. NSF grant DMR 9733160 and by the Georgia Institute of Technology. N.T. thanks the Ph.D. program of Xiamen University for support.

Supporting Online Material

www.sciencemag.org/cgi/content/full/316/5825/732/DC1
Materials and Methods
Figs. S1 to S13
References

29 January 2007; accepted 12 March 2007
10.1126/science.1140484